PNAS

www.pnas.org

Supplementary Information for

Self-assembly of photonic crystals by controlling the nucleation and growth of DNA-coated colloids

Alexander Hensley, William M. Jacobs, W. Benjamin Rogers

William M. Jacobs; E-mail: wjacobs@princeton.edu
W. Benjamin Rogers; E-mail: wrogers@brandeis.edu

This PDF file includes:

Supporting Information Text

1. Synthesizing DNA-coated colloids

We prepare DNA-grafted colloidal particles using a combination of strain-promoted dibenzocyclooctyne (DBCO) click chemistry and physical grafting, following a modified version of the methods described by Pine and co-workers(1). In brief, we functionalize polystyrene-block-poly(ethylene oxide) (PS-b-PEO) with an azide group, adsorb the azide-modified PS-b-PEO onto the surface of polystyrene colloidal particles, and then attach DBCO-modified DNA to the PS-b-PEO via click chemistry. We functionalize PS-b-PEO (M_w =6500 g/mol and 3800 g/mol, Polymer Source, Inc.) with an azide group. First we attach a mesyl group via methanesulfonyl chloride (471259, Sigma-Aldrich), and then we replace the mesyl group with an azide group N_3 via sodium azide (S2002-5G, Sigma-Aldrich). Next, we incorporate the PS-b-PEO-N_3 onto the surface of 600-nm-diameter polystrene particles (S37495, Molecular Probes) by swelling the particles with tetrahydrofuran (THF, 99.9% inhibitor free 401757, Sigma-Aldrich) in an aqueous solution of PS-b-PEO-N_3. Next, we add additional deionized (DI) water to the solution and wait for an hour in order to deswell the particles. We then wash the particles five times by repeated centrifugation and resuspension in DI water. Finally, we attach DBCO-modified DNA molecules via a click reaction with the azide groups in a solution of tris-EDTA buffer (pH 8), pluronic F-127 (51181981, Sigma-Aldrich), and sodium chloride. We rotate the reaction mixture end-over-end in an oven at $60°$C for 24 hours and then wash the particles five times in DI water. We store the particles at a concentration of 1% (v/v) in DI water at $4°$C. The two DNA sequences are 5'-(T)$_{51}$-GAGTTGCGGTAGAC-3' and 5'-(T)$_{51}$-AATGCCTGTCTACC-3'.

2. Making droplets with microfluidics

We use PDMS-based microfluidics to prepare colloid-filled droplets. The droplets are stabilized by a fluorinated surfactant (RAN) suspended in fluorinated oil (HFE-7500) at a concentration of 2%. The droplets contain an aqueous solution of colloidal particles, 5 mM Tris/0.5 mM EDTA buffer, and 500 mM NaCl.

Design. We use a PDMS-based, microfluidic drop maker. Our device is comprised of two inlets for different aqueous phases that combine on-chip, and one inlet for an oil phase which splits into two opposing streams that terminate perpendicular to the combined aqueous stream (Figure S1a). The two aqueous phases are combined at a Y-shaped junction. The combined aqueous phase is then pinched off from two sides by the oil phase to form droplets(Figure S1b). We collect the resulting droplets in an Eppendorf microcentrifuge tube.

Manufacture. We use standard soft-lithography techniques to manufacture our microfluidic drop-makers. We spincoat liquid SU-8 photoresist (SU-8 2075, MicroChem) onto a silicon wafer (3-76-024-V-B, Silicon Materials Inc.) and then place a photomask (Output City) on the wafer. We use a Manual Mask Aligner System (ABM-USA) to make the SU-8 thickness 80 μm and then we cure the photoresist with UV light. Next we wash away the uncrosslinked photoresist with propylene glycol monomethyl ether acetate (484431, Sigma-Aldrich) to create a negative master of the microfluidic device on the wafer.

We then create a mold from the master. We line a Petri dish with aluminum foil and place the etched wafer into the dish. We mix polydimethylsiloxane (PDMS) and crosslinker (1673921, Dow Chemical Company) in a 10 to 1 (w/w) ratio with a Thinky AR-250 planetary centrifugal mixer and pour it into the Petri dish. We degas the sample and then place it in an oven at 70 degrees centigrade for at least 2 hours to cure. We separate the cured PDMS from the master with a hobby knife and create inlet and outlet channels with a core sampling tool (69039-07, Electron Microscopy Sciences). Finally, we bond the PDMS device to a glass microscope slide (2947-75X50, Corning) with oxygen-plasma treatment for 45 seconds.

Operation. We use syringe pumps to operate our microfluidic device to produce monodisperse droplets containing colloidal suspension (Figure S1a). First, we make the channels of the microfluidic device hydrophobic by flushing them with Aquapel (B004NFW5EC, Amazon), leaving it for 30 seconds, and then flushing the channels out again with air to remove the Aquapel. We repeat the process with HFE-7500 oil and then air. Finally, we flow oil and aqueous buffer through their respective inlets to ensure the device functions properly. Specifically, we control the flowrates of three 3-ml syringes independently with syringe pumps (98-2662, Harvard Apparatus) connected to the device via tubing (06417-11, Cole-Palmer) that is slightly larger in the diameter than the holes to ensure a snug fit. One syringe feeds in the HFE-7500 (3M) with 2% RAN fluorosurfactant (008-FluoroSurfactant-5wtH-20G, RAN Biotechnologies). The other two syringes feed in aqueous solutions, which are combined on-chip (Figure S1B). One of the aqueous phases contains 1M NaCl in 1xTE buffer (1 mM EDTA/10 mM Tris), and the other contains either DI water or the DNA-coated particles suspended at twice the desired volume fraction in DI water. We use flow rates of 800 μl/hr for the oil phase and 400 μl/hr for each of the aqueous phases to obtain droplets with diameters of roughly 60 μm.

Due to the small amount of DNA-coated colloids that we produce, we cannot fill the entire syringe with colloidal suspension. Therefore, we use a method to minimize the volume of DNA-coated colloids needed for a given experiment. Specifically, we fill a syringe with HFE-7500, then we place the end of the tube connected to this syringe into an Eppendorf containing the colloidal suspension and use the syringe pump in reverse to pull a 10-μl-volume plug of colloidal suspension into the tube. We then pull a millimeter-long plug of air into the tube followed by enough 1xTE to fill approximately 0.5 m of tubing. This extra volume of buffer ensures that the droplets are uniform before our colloidal suspension passes through the microfluidic device. Since the particle-filled fluid is separated by a cushion of air on both sides, the particles move through the tubing and the device as a uniform plug and do not spread due to Taylor dispersion. We collect the resulting droplets in an Eppendorf microcentrifuge tube at the exit of the outlet tubing. These droplets remain stable in solution for a period of many months. Though the droplets are stable for months, we use them within a week to minimize any irreversible aggregation that might happen over long periods of time.

Alexander Hensley, William M. Jacobs, W. Benjamin Rogers
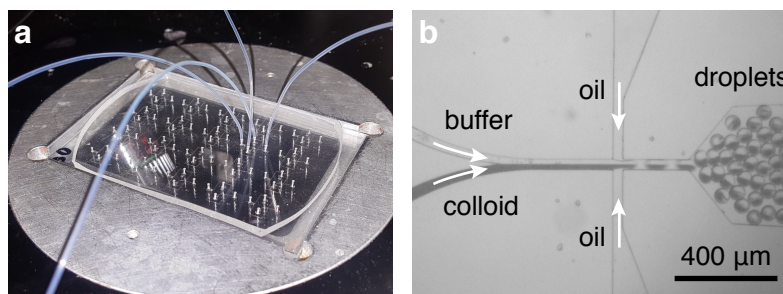
Fig. S1. Photographs of the microfluidic chip and the device under operation. (**a**) A photograph of the droplet-maker on a microscope with connected inlet and outlet tubes. The chip contains an array of 24 identical devices with one in use at any given time. The device has four tubes coming out of it, two are the inlets for the two components of the aqueous phase, one is the inlet for the oil phase, and one is the outlet for the droplets. The inlet tubes lead to three computer controlled syringe pumps and the outlet leads to an Eppendorf tube. (**b**) A brightfield micrograph of a device in use. The two aqueous inlet streams meet into a single stream before becoming squeezed into droplets by the oil phase. The droplets exit via an output tube. The central channels are roughly 50 μm in width. The arrows represent the direction of fluid flow.

3. Conducting nucleation and growth experiments

We use optical microscopy to conduct droplet-based measurements of crystal nucleation and growth. The basic workflow includes making a sample chamber, imaging the sample using an inverted optical microscope, controlling the sample's temperature, and then recording time-lapse images as crystals nucleate and grow.

Making the sample chamber. We prepare sample chambers comprised of a rectangular capillary filled with colloidal suspension and glued to a glass coverslip. We cut a 100-μm-thick, 2-mm-wide glass rectangular capillary (5012, VitroCom) to 3 cm in length with a glass scoring pen and hold it in place with a pair of clamping tweezers. We transfer approximately 2–3 μl of colloidal suspension into the capillary using a micropipette. We fill the rest of the volume of the capillary with HFE-7500 containing 2% RAN fluorosurfactant. We add HFE-7500 to each side of the capillary such that the bulk of the droplets are in the middle of the capillary during the following steps. We then use a syringe to apply a thin line of UV curing adhesive (NOA 68, Norland), 3 cm in length, onto the center of a plasma cleaned 24 mm × 60 mm No. 1 glass coverslip (48393-106, VWR). We place the capillary directly onto the line of adhesive and press evenly to enure that the sample is flat against the coverslip. We then seal the ends of the capillary with the same adhesive. We leave the sample to cure under UV light uncovered for 30 s in order to cure the thin film, and then for another 30 min with aluminum foil covering all but the ends of the capillary to seal the ends.
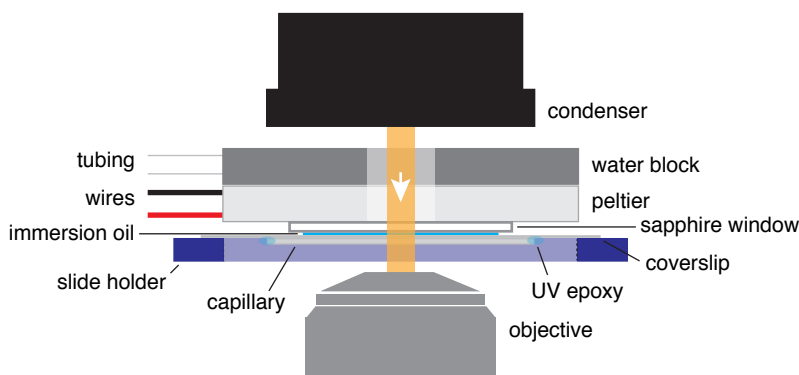
**Fig. S2.** A front facing diagram of the sample chamber and imaging setup.

Imaging the sample. We image the sample using a Nikon Eclipse Ti2 inverted microscope equipped with an LED light source (MEE55700, Nikon). We place our sample with the capillary facing down onto an acrylic frame that allows the sample to face the microscope objective without the glue or capillary coming into physical contact with the microscope stage. The frame ensures that the sample remains level and is not bent (Figure S2) as other elements are pressed on top of it. We use a 10x-magnification objective (MRD00105, Nikon) to create an image of our sample one the sensor of a CMOS camera (Phantom v9.1). We focus and center the condenser lens for Koehler illumination and then close the condenser aperture to about 25% to increase the contrast of the edges of the droplets. We use the Nikon Perfect Focus System to keep the sample in focus over the course of our experiment.

Acquiring data. We acquire digital images using a Phantom v9.1 CMOS camera controlled by the PCC 2.8 software. All images have a pixel resolution of 1632 × 1200 and a pixel size of 1.15 μm. The camera takes 14-bit grayscale images that are saved as 16-bit TIFF files in batches of 23 images at a time. We acquire images with a frame rate of 0.1 Hz.

Controlling the temperature. We control the temperature of our sample *in situ* using our temperature-controlled sample chamber and a closed-loop temperature controller. Our custom heating device is illustrated in Figure S2. Here we list the components of the device starting from the sample and moving up toward the condenser lens. On the top of the sample we place a droplet of immersion oil (MXA22166, Nikon) to create thermal contact with a sapphire window, which is connected via thermal paste (1446622, Dow Corning) to a Peltier thermoelectric cooler (TEC). The TEC module (CH-109-1.4-1.5, TE-Technology) has a central hole that allows us to image our sample in transmission. A metal waterblock placed on top of the TEC removes waste heat produced during active cooling. Capillary forces due to the thin layer of immersion oil between the sapphire window and coverslip hold the assembly together.

A temperature controller monitors the sample temperature using a temperature-sensitive resistor attached to the surface of the Peltier heater. The control loop adjusts the current running through the Peltier heater to achieve a user-specified setpoint temperature. We estimate the fluctuations in the sample temperature to be $\pm 0.02^\circ C$.

We run a specific temperature protocol to collect nucleation-rate and crystal-size information in a consistent manner. We begin by determining a temperature at which the DNA-grafted particles in the droplets disaggregate, also referred to as melting. We then lower the temperature, or quench, to such a degree that spontaneous aggregation occurs. If spontaneous aggregation does not occur at the chosen temperature we melt the sample and try a lower temperature. We then begin the experiment by melting the sample and quenching it to the temperature at which we found spontaneous aggregation. After each quench, we remelt the sample for 20 minutes and then quench to a temperature that is $0.05^\circ C$ higher than the previous quench. We repeat this process until there is no observable assembly over the full duration of the experiment. Each quench is held for one hour. If less than 90% of the droplets have formed a crystal after one hour, the quench is held for total duration of $4\ hr$.
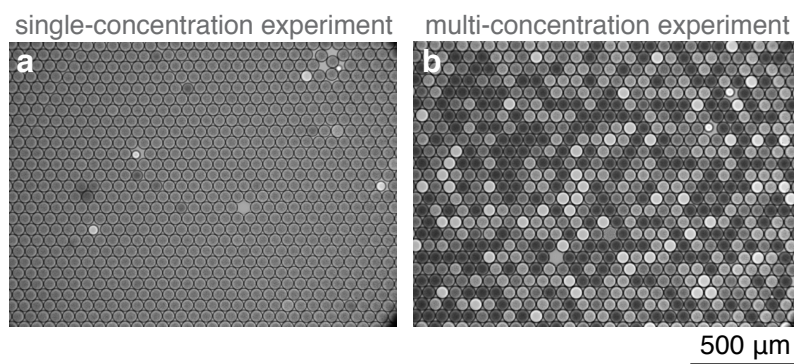
Fig. S3. Micrographs of the two kinds of experiments we perform. (**a**) An example image of a single-concentration experiment of droplets with a particle volume fraction of 0.50%. (**b**) An example image of a multi-concentration experiment with roughly an equal number of droplets of 1.00%, 0.50%, and 0.25% colloids (v/v), as well as a small number of 0% droplets. The droplets with lower volume fractions appear brighter than those with higher concentration. There are roughly 600 droplets in each image. The temperature in both cases is held above the colloid melting temperature.

Running the experiment We perform two types of droplet-based experiments: one in which all droplets have the same colloid concentration and another in which we image four different droplet types simultaneously. The single-concentration experiment enables us to image roughly 600 nearly identical droplets simultaneously (Figure S3a). Imaging 600 droplets at once provides good statistical power. However, using droplets of a single concentration has two drawbacks: 1) it is difficult to compare experiments performed at different colloid concentrations due to the finite accuracy of our temperature controller; and 2) it is difficult to calibrate variations in the transmitted light intensity that come from drift in the illumination. Therefore, we perform a second type of experiment that uses droplets of four different concentrations simultaneously to remedy these two issues (Figure S3b). The droplets in the multi-concentration experiment contain four different colloid concentrations: 0%, 0.25%, 0.50%, and 1.00% (v/v). We add roughly equal proportions of the 0.25%, 0.5%, and 1% droplets, as well as a small number of colloid-free droplets. The primary advantage of the multi-concentration experiment is that it allows us to make direct comparisons between different concentrations, ensuring that the entire system is at the same temperature. We use the empty droplets for calibration as they should not change in intensity over time. Thus changes in intensity in the empty droplets come from systemic changes to our imaging setup and can be used to correct the intensities of the other droplets. The disadvantage of this experiment compared to the single-concentration experiment is that the statistical power for each droplet concentration cut by a factor of three. However, we compared the measured nucleation rates for a single-concentration experiment with 0.50% colloids to a multiconcentration-experiment and did not find any noticeable differences.

4. Running temperature-ramp experiments

We perform all temperature-ramp experiments in a PCR thermal cycler. In brief, we prepare an emulsion of colloid-filled droplets in 200-microliter-volume PCR tubes, as decsribed above. We place the PCR tubes in a thermal cycler (Bio-Rad C1000 Touch Thermal Cycler) and program a linear temperature ramp, which begins at an initial temperature that is above the colloid melting temperature. We also place a thermistor, which is potted in a dab of thermal compound, in a PCR tube in a neighboring well to monitor the temperature throughout the annealing protocol. The C1000 Touch thermal cycler has a minimum temperature step size of $0.1^\circ C$. Therefore, we specify the average ramp rate by setting the duration of each step in the protocol. More specifically, we vary the step length from 8 hr to 30 min, yielding average ramp

Alexander Hensley, William M. Jacobs, W. Benjamin Rogers

rates that vary from 0.0125°C/hr to 0.2°C/hr. To maintain as uniform temperature as possible in our emulsion and to minimize evaporation, we set the lid temperature of the thermal cycler to 55°C.

After annealing, we measure the probability of forming a single crystal in each drop using optical microscopy. We prepare a sample chamber of crystal-filled droplets, as described above, and image them on a Nikon Eclipse Ti2 inverted microscope. Next we acquire images of 2–3 fields of view, which contain an unbiased sample of roughly 1000 droplets. Finally, we manually inspect each droplet and count the number of distinct crystal domains. Any anomalously large droplets, which we attribute to coalescence sometime during the experiment, are excluded from the analysis.

## 5. Image and data analysis

We extract quantitative information on each of the droplets in the image sequences using image-analysis and data-analysis routines written in MATLAB.

Droplet identification and tracking. We find the droplet positions and radii for each image using a sequence of image transforms. First we apply a Gaussian filter to the raw images (Figure S4a) to smooth out the high frequency noise. Then we perform a Laplacian convolution to accentuate the edges of the droplets and threshold the image to remove low-intensity noise and create a binary image (Figure S4b). Next we remove any small disconnected features within the droplets (Figure S4c). We perform a Euclidean distance transform to convert the binary image into a grayscale image with a bright spot in the center of every droplet (Figure S4d). The central pixel value is roughly equal to the radius of the droplet in units of pixels. Lastly, we use a centroiding routine to determine the droplet centers and radii(2) (Figure S4e). For each image, we create a matrix that contains the x and y positions, as well as the droplet radii. Finally, we track the droplets as a function of time using the particle-tracking algorithm developed by Crocker and co-workers (2).
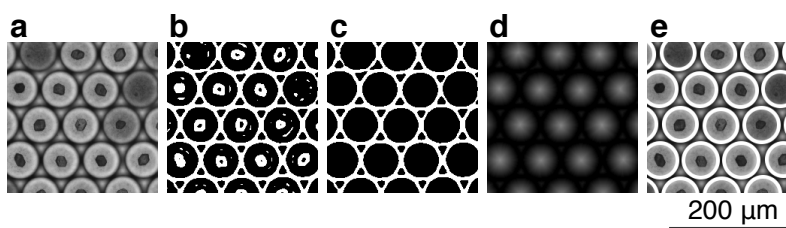
Fig. S4. The image transformations done to identify droplet locations efficiently. (**a**) The raw image. (**b**) We apply a gaussian blur to the image to dampen high frequency noise, then apply a Laplacian transform to accentuate the droplet edges, and then apply a threshold to binarize the image. (**c**) We remove all small contiguous features leaving only the connected mesh of droplet edges. (**d**) We calculate a distance map showing the distance each pixel is to the nearest droplet edge pixel, where the brightest pixels are at the droplet centers. (**e**) We use a centroiding routine to identify the droplet locations and radii.

Separating the droplets by concentration. We identify droplets of different concentration by their transmitted light intensities. Figure S5a shows a histogram of the relative droplet intensities for a sample containing four different droplet concentrations: $0.00\%, 0.25\%, 0.50\%, 1.00\%$. Droplets with a higher concentration appear darker. We separate the populations by applying thresholds between the four different peaks. Figure S5b shows the droplets color coded according to their inferred concentrations from the histogram. Visual inspection shows that all droplets are classified correctly.
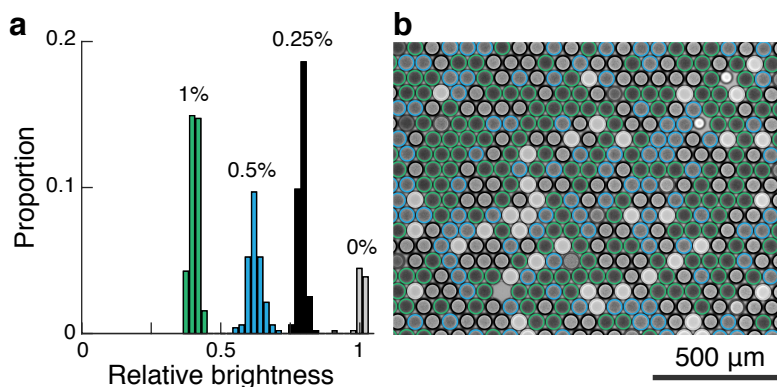

Fig. S5. Identification of droplet concentrations from their relative brightness. We bin four different populations of droplets by their transmitted intensities. (**a**) A histogram of the transmitted intensities of droplets relative to the intensity transmitted through empty droplets. The data is multimodal with each separate cluster in the histogram representing a different concentration. Dark gray bars represent droplets that are ambiguous and are therefore omitted from our analysis. (**b**) An image from the experiment in which the droplets are highlighted according to their concentration by the colors in (**a**).

Crystal identification. We identify crystals within the droplets using a contrast based method. We measure the intensity of each droplet $I(t)$ by averaging the pixel values within an annulus of a user-defined inner and outer radius around the droplet center. We use an annulus instead of the entire droplet to ensure a uniform path length. To determine if a crystal is present we identify all pixels in each droplet that have an intensity that is less than 0.65 times the mean annulus intensity. If there is a contiguous block of these dark pixels greater than a threshold size of 15 pixels, we identify this droplet as containing a crystal. This information is appended to the position and radius matrix for each droplet.

Identifying nucleation events. We determine the time at which crystals first nucleate using a rolling analysis of 100 sequential frames for each droplet, starting at frame one. If a crystal is identified in at least 65 of the 100 frames, we define the first instance of the crystal as the nucleation time. If fewer than 65 of the 100 frames contains a crystal, we slide the 100-frame window forward by one frame and repeat the analysis. We use the sliding window to minimize errors due to any false positives.

Quantifying growth. We analyze the growth of crystals by comparing the transmitted light intensity, $I(t)$, of each droplet over time to the transmitted intensity of an empty droplet I_0. We first create a calibration image to obtain a reference intensity I_0 at each point in the image plane. Briefly, we take an image of the system at a low temperature at which the particles are completely aggregated, leaving zero free particles in the bulk (Figure S6a). We then mask out the aggregates using a threshold (Figure S6b), and compute the average intensity of each droplet within the user-specified annulus. The intensity of the annulus should be that of an empty droplet, as there are no particles in the fluid phase in this calibration image. Next we construct two-dimensional map of $I_0(x, y)$ at each pixel using two-dimensional interpolation (Figure S6c). We use this calibration image to compute the relative intensity $I(t)/I_0$ of every droplet in every frame.
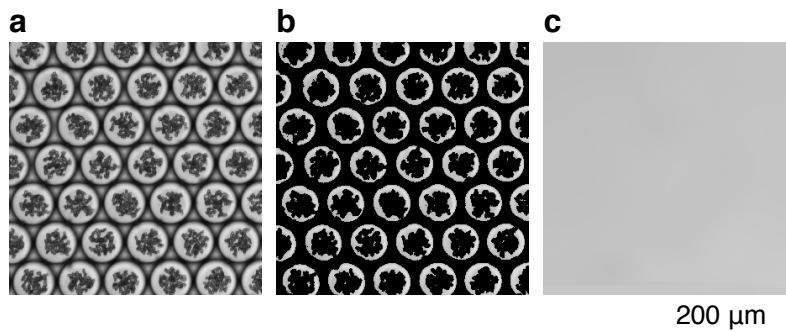
Fig. S6. Determining the reference intensity. (**a**) We acquire a calibration image in which all of the particles are aggregated in the center of the droplets. We threshold the image to remove the aggregated particles (**b**) and then average the intensity of the remaining pixels. (**c**) We interpolate the average transmitted intensities from (**b**) to create a two-dimensional map of the reference intensity $I_0(x, y)$ at every location on the image.

We correct for any temporal variations in the reference intensity using the transmitted intensity of the empty droplets. Over the full duration of our experiments, which can take multiple days to complete, the illumination can change with time, either due to small changes in the focus or variations in the lamp intensity. We take advantage of the fact that the relative intensity $I(t)/I_0$ of the empty droplets should not vary with time to correct for any intensity drift. Specifically, we divide the relative intensity $I(t)/I_0$ of each droplet by the value $I(t)/I_0$ averaged over all the empty droplets in each frame.

Figure S7 shows an example of an uncorrected and a corrected trajectory. The relative intensity of the droplet increases as the crystal grows, depleting monomers from the bulk. There are clearly spurious features in the trajectory. When we compare the relative intensity of the droplet to the average behavior of the empty droplets, we find the same spurious features (Figure S7a). Because the empty droplets should always have a relative intensity of 1, and any deviations from that intensity value are systemic to all the droplets, we can be correct the relative intensities of the droplets by normalizing them with respect to the empty droplets (Figure S7b).

We use the ratio of the transmitted intensity to the reference intensity to calculate the gas density within each droplet as a function of time. We assume single scattering and infer the number density of the gas phase $\rho(t)$ from the relative intensity $I(t)/I_0$:

$$\frac{I(t)}{I_0} = \exp\left[-\rho(t)\sigma L\right], \tag{1}$$

where σ is the scattering cross section, and L is the path length. Although we do not know σL a priori, we can infer the value of the product σL from the transmitted light intensities at time $t = 0$, when all of the particles are known to be in the gas phase. Then we use the fact that the quantity σL is a constant in time to then infer the number density of the gas phase $\rho(t)$ within each droplet for all subsequent frames (Figure S7c).

We confirm that the transmitted light intensity is governed by single scattering and obeys Equation 1. Specifically, we fit a single value of σL at $t = 0$ to a set of roughly 600 droplets with three particle volume concentrations. We then use this value to infer the colloid volume fraction in each drop individually (Figure S8). We find that the mean values of the measured volume fractions match the intended volume fractions that we prepared. Furthermore, our measurements also provide an upper bound on the droplet-to-droplet variations in the concentration, which vary by roughly ±6%. This value is most likely an upper bound since it includes contributions due to small spatial variations in the lamp intensity in addition to variations in the concentration from droplet to droplet.

Alexander Hensley, William M. Jacobs, W. Benjamin Rogers
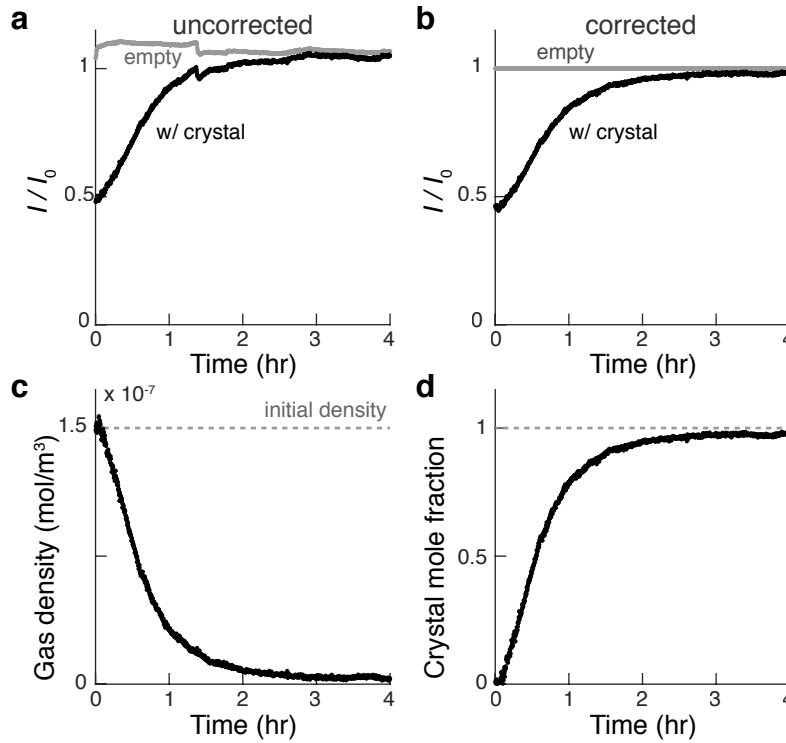
Fig. S7. Inferring the gas density and crystal mole fraction from the transmitted light intensity. (**a**) The relative transmitted light intensity $I(t)/I_0$ as a function of time for an empty droplet and a droplet containing a growing crystal. Variations in I/I_0 for the empty droplet are artifacts from focus drift or fluctuations in the lamp intensity. The same variations are seen in I/I_0 for the droplet with a crystal. The monotonic increase in $I(t)/I_0$ for the droplet with a crystal is due to the depletion of monomers in the gas phase from crystal growth. (**b**) Artifacts in I/I_0 are corrected by dividing the relative intensity by the relative intensity transmitted through the empty droplets. (**c**) We infer the gas density as a function of time from the corrected relative intensities using Equation 1. (**d**) We calculate the crystal mole fraction χ from the gas density in (**c**) according to $\chi = (\rho_0 - \rho(t))/\rho_0$.
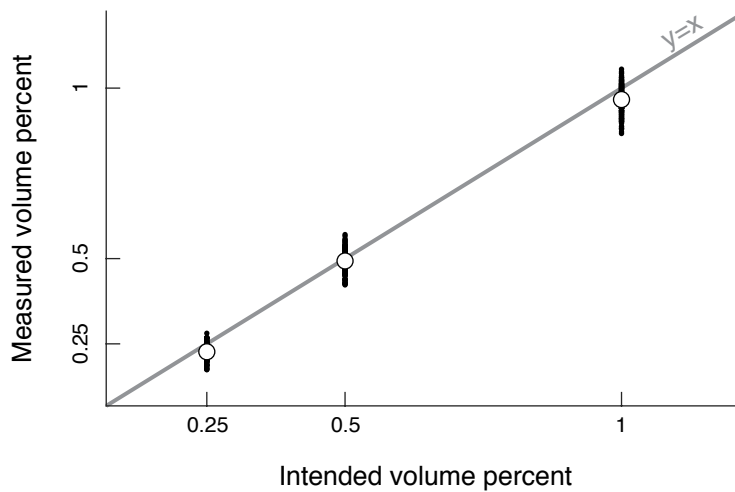
Fig. S8. A single-scattering model accurately captures the scattered light intensities. After fitting a single value of σL, the product of the scattering cross section σ and the pathlength L, we measure the volume fractions of three populations of droplets with volume fractions of 0.25%, 0.5%, and 1%. Black points show the measured volume percent for individual droplets; white points show the average volume percentage of roughly 200 droplets of a given concentration. The gray line shows $y = x$, which corresponds to perfect agreement between our experiments and our single-scattering model. The small deviations that we see in the mean volume fraction likely result from small errors in pipetting or small imbalances in the flowrates in our microfluidic device.

Finally, assuming a single crystal forms within each drop, we infer the size of the crystal within each as a function of time from the gas density. Specifically, we determine the number of particles in the crystal N from $N(t) = [\rho_0 - \rho(t)]V_{\mathrm{drop}}$, where ρ_0 is the initial number density of the gas phase at $t = 0$ and V_{drop} is the volume of a droplet. We also calculate the mole fraction of the crystal phase $\chi(t)$ from $\chi(t) = [\rho_0 - \rho(t)]/\rho_0$. Figure S7d shows the inferred crystal mole fraction within a single drop as a function of time.

Correcting for temperature offsets. Although our temperature controlled sample chamber has a spatial uniformity and precision of roughly 0.01 °C, we find that the accuracy of the absolute temperature can vary by 0.1–0.2 °C from run to run. We attribute these shifts in the absolute temperature to slight differences in the thermal contact between the various layers of our sample chamber (Fig. S2). We correct for systematic errors in the absolute temperature by shifting the temperatures to align our measurements of the fraction of droplets that fail to nucleate at the end of a given quench (Figure S9). For example, Figure S9a shows the fraction of 0.25% volume fraction droplets that fail to nucleate by the end of a quench as a function of the temperature for two different runs. As the temperature increases, a smaller number of droplets nucleate a crystal within the finite duration of the quench. We see the same trend for both runs, but one run is shifted to higher temperature with respect to the other by 0.07 °C. We attribute this shift to a systematic error in the measurement of the absolute temperature. Therefore, we offset the temperatures to align the fraction uncrystallized as a function of temperature for each independent run (Figure S9b).
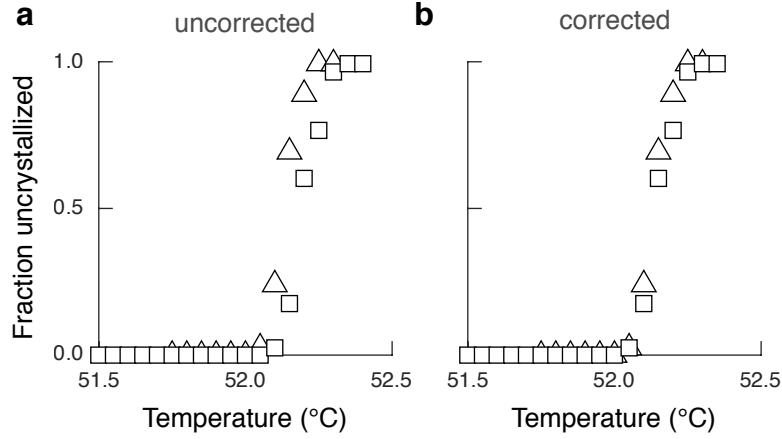
Fig. S9. We correct for small systematic errors in the absolute temperature from run to run. More specifically, we shift the temperatures of a given run by a constant offset to align the fraction of uncrystallized droplets that remain after four hours. We attribute the systematic error in the absolute temperature, which is typically around 0.05 °C, to small differences in the thermal contact between the thermoelectric cooler and the sample (Fig. S2). (**a**) shows the fraction of droplets that have not yet nucleated after four hours for two different runs of our experiment before any correction. Different shaped symbols correspond to different runs of the experiment. (**b**) shows the fraction of droplets that have not yet nucleated after four hours post correction. The squares have been shifted by −0.05 °C.

Measuring the equilibrium gas density. We infer the gas density at coexistence from our measurements of the transmitted light intensity. Figure S10a shows example snapshots of equilibrated crystals at a variety of temperatures. For each initial colloid concentration and temperature, we fit Equation 26 to the growth trajectories from individual droplets, taking ρ_{eq}, D, and t_{offset} as free parameters. We then average the gas densities at coexistence over all droplets at each temperature, and take this value to be the gas density at equilibrium. We do not notice any systematic dependence of the equilibrium gas density on the initial colloid concentration: All three initial concentrations have roughly the same gas density at coexistence at the same temperature.

Our measurements show that the gas density at coexistence increases exponentially with increasing temperature. Figure S10b shows measurements of the equilibrium gas density as a function of temperature. Over a range of roughly 0.25 degrees Celsius, we see that the equilibrium gas density increases by roughly an order of magnitude upon increasing temperature. Furthermore, when plotted on semilog axes, we see that the gas density increases roughly linearly between 52–52.25 degrees Celsius. We note that the equilibrium density continues to decrease at even lower temperatures. However, those low concentrations are below the detection limit of our experimental approach. We determine our detection limit by calculating the standard deviation of the measured bulk concentration of droplets for deep quenches where nearly all of the particles are contained in a dense cluster. For each droplet in the deepest quench of a 1.00% run, we calculated the standard deviation of the bulk concentration for the final 100 frames of the quench and took the mean of all these standard deviations as our minimum detection threshold. We calculate a threshold bulk concentration of 10^{-9} mol/m³ and do not consider concentrations at or below this threshold when we perform our fit in Figure S10b. For the $32\,\mu$m in radius droplets we use, this concentration corresponds to around 80 particles.

6. Modeling nucleation and growth

A. Equilibrium thermodynamics. Under the conditions investigated in the experiments, the colloid gas phase can be treated as an ideal gas, since the mean free path in the gas phase is approximately ten times the particle radius. The equilibrium gas density, ρ_{eq}, in coexistence with the crystal phase is fit to the equation (Figure S10a,b)

$$\log\left[\rho_{\text{eq}}(T)/\text{M}\right] = 10.5(T/^\circ\text{C}) - 573.4. \tag{2}$$

The measured gas-phase density is twice the density of each of the two distinct colloidal species. From these measurements, we define the temperature-dependent supersaturation, S,

$$S(T) = \frac{\rho}{\rho_{\text{eq}}(T)}, \tag{3}$$

Alexander Hensley, William M. Jacobs, W. Benjamin Rogers

Parameter	Estimated value	Description
d	$6 \times 10^{-7}\,\mathrm{m}$	colloid diameter
δ	$1.5 \times 10^{-8}\,\mathrm{m}$	colloid–colloid interaction range
ϕ	0.74	crystal packing fraction
z	8	crystal coordination number
D	$1 \times 10^{-12}\,\mathrm{m^2 s^{-1}}$	gas-phase diffusion constant
κ	$0.1\,\mathrm{s^{-1}}$ (3)	rolling/sliding diffusion rate
V_{drop}	$1 \times 10^{-13}\,\mathrm{m^3}$	droplet volume

Table S1. Descriptions and estimated values of parameters used in the DNA-grafted colloid crystallization model.

Variable	Description
ρ	colloidal gas-phase density
ρ_0	initial colloidal gas-phase density
ρ_{eq}	equilibrium colloidal gas-phase density
S	supersaturation
σ	$\sigma \equiv S - 1$
ρ_{c}	colloidal crystal-phase density
N_{c}	number of colloids in the crystal phase
R	radius of crystal nucleus
v	growth velocity in the direction normal to the surface of the crystal nucleus
v_∞	diffusion-limited growth velocity in the direction normal to the surface of the crystal nucleus
λ	mean free path length in the colloidal gas phase
k_{att}	net attachment rate of a single particle to the emerging crystalline lattice
K	equilibrium constant for an unstable adsorbed colloidal particle
α	attachment coefficient
α_{diff}	$\alpha_{\mathrm{diff}} \equiv \rho_{\mathrm{eq}} D S / \rho_{\mathrm{c}} v_\infty R$
k_{n}	nucleation rate
$k_{\mathrm{n,0}}$	nucleation-rate prefactor
$\Delta G^{\ddagger}$	free-energy difference between the top of the nucleation barrier and the metastable colloidal gas phase
γ	colloidal crystal–vapor surface tension
ε	free energy per colloid-colloid contact
ξ	$\xi \equiv \gamma / \rho_{\mathrm{c}} k_{\mathrm{B}} T$, Gibbs–Thomson correction
τ_{g}	time required for a single nucleus to grow large enough to suppress further nucleation

Table S2. Descriptions of important variables in the DNA-grafted colloid crystallization model.

which is the same for each of the colloidal species in the equimolar mixture.

We model the DNA-grafted colloids using the hard-sphere square-well model with colloid diameter d and square-well width δ (see Table S1). The coordination number in the crystal phase is $z = 8$, which is the number of 'unlike' contacts between the two particle species in the CuAu-FCC crystal structure. Using the cell model presented in Reference (4), we estimate the binding free energy per colloid–colloid contact, $\varepsilon(T)$, according to (Figure S10c)

$$\frac{\varepsilon(T)}{k_{\mathrm{B}} T} = \frac{2\left\{\log\left[\rho_{\mathrm{eq}}(T)\delta^3\right] + 1\right\}}{z}. \tag{4}$$

We thus expect the binding free energy $|\varepsilon|$ to be roughly 4 to 5 $k_{\mathrm{B}} T$ over the range of temperatures used in the experiments. This range of binding free energies is consistent with previous measurements of the colloid–colloid binding free energy (5, 6). Nonetheless, we note that the absolute value of the binding free energy predicted by the cell model, which influences our prediction of the crystal–vapor surface tension, $\gamma(T)$ (see Sec. B), is sensitive to our estimate of the parameter δ. Consequently, we focus on the temperature dependence of ε and γ, which is independent of δ, when comparing the cell model to our experimental measurements.

B. Attachment kinetics. We model the attachment of a free colloidal particle to a crystalline nucleus via a two-step process: First, the particle adsorbs onto the surface of the cluster, and second, the particle diffuses along the surface to a stable position within the crystalline lattice. Under mild supersaturation, attachment of a particle to a cluster consisting of i colloids can be modeled as an activated process involving an unstable intermediate, $(i+1)^{\dagger}$:

$$i \qquad\qquad (i+1)^{\dagger} \qquad i+1$$

Alexander Hensley, William M. Jacobs, W. Benjamin Rogers
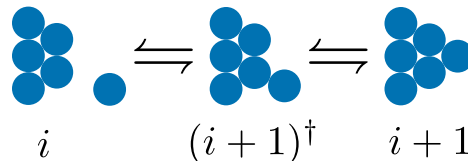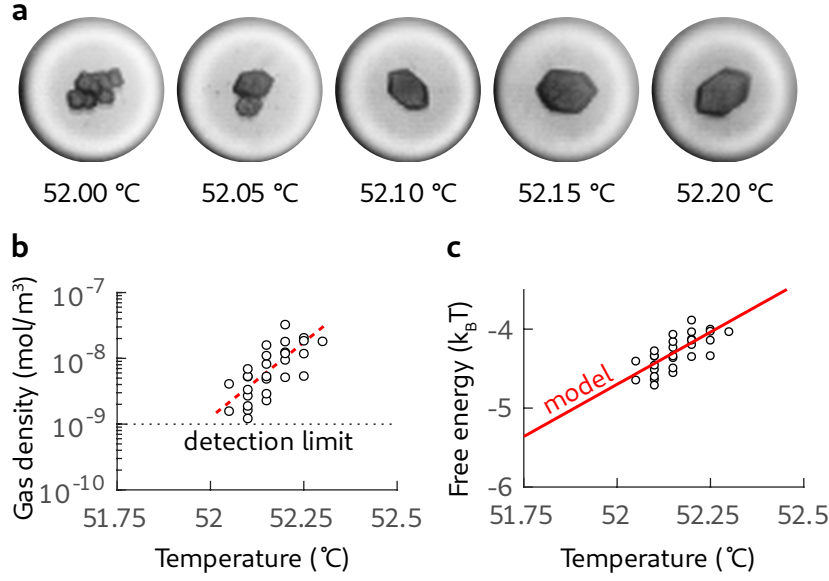
Fig. S10. The equilibrium bulk concentration is recorded at each temperature and fit to a line to infer the supersaturation for all experiments. (**a**) Sample crystals grown to their fullest extent for a variety of temperatures show that as the temperature is increased, the larger equilibrium bulk concentration makes the droplet bulk appear darker. (**b**) The equilibrium concentration with respect to temperature. We only plot equilibrium concentrations in excess of 10^9 mol/m^{-3}, as that is our detection limit below which the noise in our analysis is greater than the value of the concentration. A linear fit is indicated by the dashed red line. (**c**) The estimated binding free energy between a pair of colloidal particles using the model presented in Eq. (4).

This two-step process can be described by the reaction scheme

$$i \underset{v_\infty/dK}{\overset{v_\infty/d}{\rightleftarrows}} (i+1)^\dagger \overset{\kappa}{\rightarrow} (i+1). \qquad [5]$$

The first step involves the attachment of a new colloid by fewer than $z/2$ bonds at the diffusion-limited rate v_∞/d, which we express in terms of the growth velocity in the direction normal to the surface of the cluster, v_∞. The diffusion-limited rate follows the scaling relation (7)

$$\frac{v_\infty}{d} \sim \frac{D}{\lambda^2} \simeq D\rho^{2/3}, \qquad [6]$$

where D is the self-diffusion coefficient and $\lambda \sim \rho^{-1/3}$ is the mean free path length in the colloidal gas phase. Dissociation occurs according to detailed balance and the equilibrium constant K. The second step, associated with the rate κ, reflects the need for a colloid to roll or slide into place once in the state $(i+1)^\dagger$; rolling/sliding can be described by diffusion in two dimensions (8, 9), and $1/\kappa$ is the characteristic time required for a colloid to roll or slide from one lattice position to another. At coexistence between the colloidal gas and crystal phases, the effective rate (i.e., the reciprocal of the mean first passage time) for transitioning from state i to state $i+1$ is

$$k_{\text{att}} = \frac{\kappa}{(1+K^{-1}) + \kappa d/v_\infty}. \qquad [7]$$

Importantly, k_{att} does not depend strongly on the diffusion-limited rate when $K \ll 1$ and $\kappa \lesssim v_\infty/d$, i.e., when the activated intermediate state is unstable and the rolling/sliding rate is comparable to or slower than the diffusion-limited attachment rate.

Again invoking the cell model (4), we estimate the equilibrium constant for attaching a colloid at a non-crystalline position according to

$$K(S) \approx S(\Omega/\delta^3) \exp(\Delta\varepsilon^\dagger/k_B T), \qquad [8]$$

where $\Omega \approx \delta d^2$ is the free volume in the intermediate state $(i+1)^\dagger$, $\Delta\varepsilon^\dagger \simeq (z/2 - z')\varepsilon$, and z' is the number of bonds formed in the intermediate state. Taking $\varepsilon \approx -4.5 k_B T$ and $z' = 1$, we estimate $K(S=1) \approx 10^{-3}$ for the attachment of a particle to a small nucleus with high surface curvature, since in this case the adsorbed particle is likely to make only a single bond with the cluster. When attaching to a nearly flat crystalline interface, an adsorbed particle may make a greater number of bonds, leading to a larger value for K.

C. Classical nucleation theory. We assume that the nucleation rate density for homogeneous nucleation follows the classical nucleation theory (CNT) form (10)

$$k_n = k_{n,0}(\rho, T) \exp\left(-\Delta G^\ddagger/k_B T\right), \qquad [9]$$

where $k_{n,0}$ is referred to as the nucleation-rate prefactor and $\Delta G^\ddagger$ is the free-energy difference between the top of the nucleation barrier and the metastable phase.

Alexander Hensley, William M. Jacobs, W. Benjamin Rogers

C.1. Nucleation barrier. We assume that the nucleation barrier can be described using the capillarity and spherical-nucleus approximations (11),

$$\frac{\Delta G^{\ddagger}}{k_\mathrm{B}T} = -\frac{16\pi}{3}\frac{\left[\gamma(T)\rho_\mathrm{c}^{-2/3}/k_\mathrm{B}T\right]^3}{(\log S)^2},\qquad\text{[10]}$$

where $\gamma(T)$ is the temperature-dependent crystal–vapor surface tension. The density in the crystal phase can be determined from the packing fraction, ϕ, and the colloid diameter, d, such that $\rho_\mathrm{c} = (6\phi/\pi)d^{-3}$. We comment further on the interpretation of the surface tension in Sec. B.

C.2. Nucleation rate prefactor. Following Reference (11), the nucleation prefactor can be written as

$$k_{\mathrm{n},0} = 2\rho\left[\frac{k_{+,\mathrm{eq}}(i^*)}{A(i^*)\rho_\mathrm{c}^{2/3}}\right]\left(\frac{\rho_\mathrm{c}^{-2/3}\gamma}{k_\mathrm{B}T}\right)^{1/2},\qquad\text{[11]}$$

where i^* is the critical cluster size, $A(i^*)$ is the critical cluster surface area, and $k_{+,\mathrm{eq}}$ is the rate at which the cluster grows by one particle at coexistence between the crystal and gas phases. We ignore the distinction between the two colloidal species here for simplicity. We can replace the term in square brackets with k_att evaluated at coexistence, leading to

$$\frac{k_{\mathrm{n},0}}{\rho} = 2\times k_\mathrm{att}(S=1)\times\left(\frac{\rho_\mathrm{c}^{-2/3}\gamma}{k_\mathrm{B}T}\right)^{1/2}.\qquad\text{[12]}$$

As described above, $k_\mathrm{att}(S=1)$ is expected to be essentially independent of the concentration, since $K(S=1)\ll 1$ and $\kappa\simeq D\rho_0^{2/3}$. As a result, the nucleation rate density is expected to be proportional to the colloid concentration. Empirically, we find that such a linear concentration scaling is consistent with the experimental data (see Sec. A.1). Note that this prediction differs from applications of CNT that do not account for the attachment kinetics and typically predict a stronger density dependence of the nucleation rate prefactor. For example, the diffusion-limited nucleation rate prefactor for repulsive colloids crystallizing from a dense fluid is expected to scale as $\rho^{5/3}$ (7).

D. Crystal growth. To describe crystal growth, we follow the presentation in Reference (12). The diffusion equation at steady state reduces to Laplace's equation,

$$\frac{\partial\sigma}{\partial t} = 0 = -\nabla^2\sigma,\qquad\text{[13]}$$

where we've defined

$$\sigma \equiv \frac{\rho-\rho_\mathrm{eq}}{\rho_\mathrm{eq}} = S-1.\qquad\text{[14]}$$

The growth velocity, v, of a roughly spherical crystal of radius R is

$$v = \frac{D}{\rho_\mathrm{c}}\frac{\partial\rho(R)}{\partial r} = \frac{D\rho_\mathrm{eq}}{\rho_\mathrm{c}}\frac{\partial\sigma(R)}{\partial r}\qquad\text{[15]}$$

by continuity. This velocity is assumed to follow a Wilson–Frenkel law (13),

$$v = \frac{\alpha v_\infty(R)}{S}\left[\sigma(R)-\frac{2\xi}{R}\right],\qquad\text{[16]}$$

where $\alpha\leq 1$ is the attachment coefficient, $v_\infty(R)$ is the diffusion-limited growth velocity at the crystal–vapor interface, and the term involving $\xi \equiv \gamma/\rho_\mathrm{c}k_\mathrm{B}T$ is the Gibbs–Thomson correction. Using Eq. (7), we can write the supersaturation-dependent attachment coefficient as

$$\alpha(S) = \frac{k_\mathrm{att}}{v_\infty/d} = \frac{\kappa d/v_\infty}{\left[1+K(S)^{-1}\right]+\kappa d/v_\infty}.\qquad\text{[17]}$$

Finally, to account for particle conservation within the droplet, we impose the condition

$$V_\mathrm{drop}\rho_0 - N_\mathrm{c} = 4\pi\int_{V_\mathrm{drop}}r^2\rho(r)dr = 4\pi\int_{V_\mathrm{drop}}r^2\rho_\mathrm{eq}\left[\sigma(r)+1\right]dr,\qquad\text{[18]}$$

where N_c is the number of colloids in the crystal phase.

If the droplet is large compared to equilibrium crystal size, then we can approximate the solution to this model to yield the growth velocity

$$v \simeq \frac{\alpha\alpha_\mathrm{diff}}{\alpha+\alpha_\mathrm{diff}}\left(\frac{v_\infty}{S}\right)\left[\sigma_0 - \frac{2\xi}{R} - \frac{4\pi R^3}{3V_\mathrm{drop}}\left(\frac{\rho_\mathrm{c}}{\rho_\mathrm{eq}}\right)\right],\qquad\text{[19]}$$

where $\sigma_0 = S_0 - 1$ describes the initial colloidal gas concentration, and the dimensionless parameter α_diff is

$$\alpha_\mathrm{diff} \equiv \frac{\rho_\mathrm{eq}DS}{\rho_\mathrm{c}v_\infty R}.\qquad\text{[20]}$$

Using the scaling relation for v_∞ given in Eq. (6), we can write $\alpha_\mathrm{diff} = 1/\rho_\mathrm{c}d\lambda R = (\pi/6\phi)d^2/\lambda R$. Note that Eq. (19) is valid for an equimolar mixture of two colloidal species, where σ_0 is the same for each colloidal species.
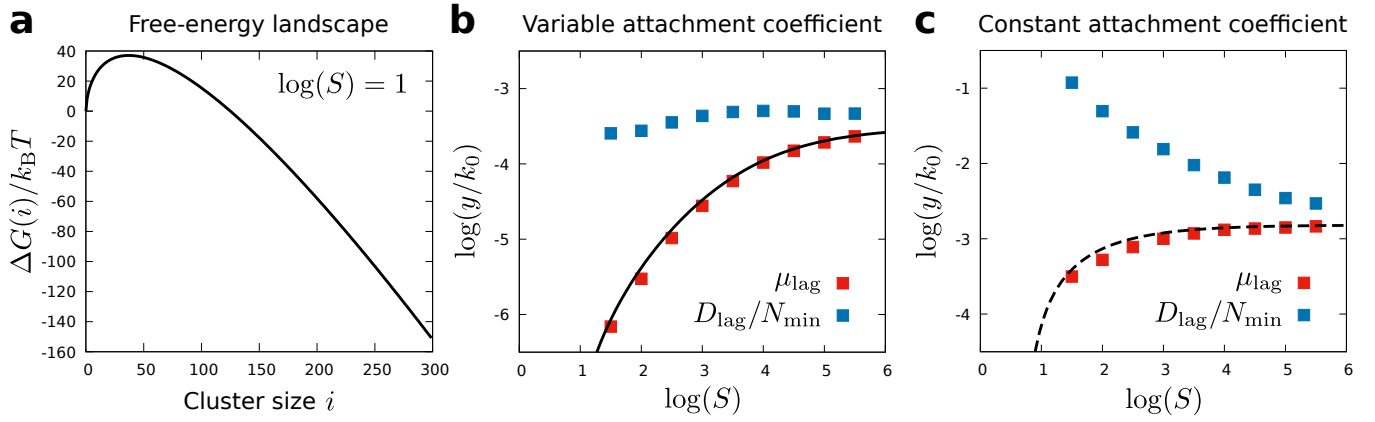
Fig. S11. Simulations of post-critical nucleus growth. (**a**) The model free-energy landscape, Eq. (23), for parameter values $\theta = 10$ and $\log S = 1$. (**b**) Fits of the mean first passage time distributions to the Inverse Gaussian (IG) distribution with the supersaturation-dependent attachment coefficient α given by Eq. (17). Both the drift and diffusion parameters, μ_{lag} and D_{lag}, are shown relative to the fundamental rate in the kMC simulations, k_0. The solid black line is the prediction given by Eq. (22). (**c**) Fits of the mean first passage time distributions to the IG distribution with a supersaturation-independent α. The dashed black line is the prediction given by the Wilson–Frenkel law with constant α.

D.1. Post-critical nucleus growth. If $\alpha_{\text{diff}} \gg \alpha$, then the growth velocity reduces to

$$v \simeq \alpha v_{\infty,0} \left[1 - \left(1 + \frac{2\xi}{R} \right) S_0^{-1} \right],$$ [21]

where $v_{\infty,0}/d$ is the diffusion-limited growth rate at the initial colloid concentration. This condition is the situation immediately following a nucleation event.

Once nucleation has occurred, the nucleus must grow to a certain size before it can be detected in the experiment. We assume that this smallest detectable cluster contains $N_{\text{min}} \approx 50$–$200$ particles (see Sec. 5). We then expect that the first passage time for the post-critical nucleus to grow to N_{min} particles will be inversely proportional to

$$v/d \simeq \left[2 + K(S_0)^{-1} \right]^{-1} \times (v_{\infty,0}/d) \left(1 - 2S_0^{-1} \right),$$ [22]

where we have substituted the critical nucleus size into the Wilson–Frenkel law and approximated $\kappa d / v_{\infty,0} \approx 1$. Note that these two approximations are not strictly necessary, but they reduce the number of fitting parameters needed below.

To examine the consequences of a supersaturation-dependent attachment coefficient on the post-critical dynamics, we perform kinetic Monte Carlo (kMC) simulations of the growth process of a post-critical nucleus on a model free-energy landscape,

$$\frac{\Delta G}{k_B T} = \theta i^{2/3} - (\log S) i,$$ [23]

where $\theta \equiv (36\pi)^{1/3} \rho_c^{-2/3} \gamma / k_B T$. The simulations generate random walks on this landscape with forward rates (i.e., $i \to i+1$) given by $k_+(i) = \alpha i^{2/3} \simeq [2 + S^{-1}K(1)^{-1}]^{-1} i^{2/3}$ and the reverse rates determined via detailed balance. Figure S11 presents simulation results using a dimensionless surface tension $\theta = 10$ and an equilibrium constant at coexistence of $K(1) = 0.02$. Using 10,000 kMC trajectories, we measure the time required for a critical nucleus to grow to $N_{\text{min}} = 300$ particles without returning to a cluster size of 1 (Figure S11a). The resulting "lag time" distributions are reasonably well described by the Inverse Gaussian (IG) distribution,

$$\text{IG}(t; \mu_{\text{lag}}, D_{\text{lag}}) = \frac{1}{\sqrt{4\pi (D_{\text{lag}}^2) t^3}} \exp \left\{ -\frac{[(\mu_{\text{lag}})t - 1]^2}{4 D_{\text{lag}} t} \right\},$$ [24]

where μ_{lag} and D_{lag} are the drift and diffusion coefficients for this first-passage process; the lag time discussed in the main text is $\tau_{\text{lag}} \equiv 1/\mu_{\text{lag}}$.

Fits to the IG distribution verify that the drift coefficient is well described by Eq. (22) when a supersaturation-dependent α is used in the expression for k_+ in the kMC simulations (Figure S11b). Furthermore, the best-fit diffusion coefficient is roughly constant, with a value approximately equal to N_{min} times the asymptotic value of the best-fit drift coefficient; thus, we can extract N_{min} from the IG fits by calculating $N_{\text{min}} \approx D_{\text{lag}}/\mu_{\text{lag}}$ for $\log(S) \gtrsim 5$. All of these features are consistent with the lag time fits to the nucleation data, as discussed below in Sec. A.1. By contrast, simulations in which α is treated as a supersaturation-independent constant, resulting in a drift coefficient proportional to the Wilson–Frenkel law given by Eq. (21), qualitatively disagree with the lag time fits to the nucleation data. In this case, the inferred drift coefficient rapidly approaches its asymptotic value for $\log(S) \gtrsim 2$, and the inferred diffusion coefficient varies strongly with the supersaturation (Figure S11c).

Alexander Hensley, William M. Jacobs, W. Benjamin Rogers

D.2. Diffusion-limited crystal growth. If $\alpha_{\text{diff}} \lesssim \alpha$, then the growth velocity is approximately

$$v \simeq \frac{D}{\rho_{\text{c}} R}\left(1 - \frac{\alpha_{\text{diff}}}{\alpha}\right)\left(\rho_0 - \rho_{\text{eq}} - \frac{4\pi R^3 \rho_{\text{c}}}{3V_{\text{drop}}}\right). \tag{25}$$

Using the relation $N_{\text{c}} = 4\pi R^3 \rho_{\text{c}}/3$, we can write the diffusion-limited growth law as

$$\frac{dN_{\text{c}}}{dt} \simeq 4\pi R D\left(1 - \frac{\alpha_{\text{diff}}}{\alpha}\right)\left(\rho_0 - \rho_{\text{eq}} - \frac{N_{\text{c}}}{V_{\text{drop}}}\right). \tag{26}$$

There are two reasons why we expect the growth process to eventually enter a regime in which $\alpha_{\text{diff}} < \alpha$. First, α_{diff} decreases as $1/R$ as the crystal grows. Second, the equilibrium constant $K(S)$ can be expected to increase as the radius of curvature of the crystal–vapor interface increases, leading to an increase in the typical number of bonds formed by an attached but as yet uncrystallized particle, z'. Thus, this model predicts a switch from kinetics-limited growth in the immediate aftermath of a nucleation event to diffusion-limited growth at later times.

Integrating Eq. (26) when $N_{\text{c}}/V_{\text{drop}} \ll \rho_0 - \rho_{\text{eq}}$, we find that the number of crystallized particles should scale as $N_{\text{c}} \sim t^{3/2}$. Once N/V_{drop} becomes comparable to $\rho_0 - \rho_{\text{eq}}$, the difference between the colloidal gas density and the gas density at equilibrium, $(\rho_0 - N_{\text{c}}/V_{\text{drop}}) - \rho_{\text{eq}}$, is expected to decay exponentially. These predictions are confirmed by fitting Eq. (26) to the growth data (see Figure 1F and Figure 3D in the main text).

7. Fitting the experimental data

A. Maximum likelihood estimation of nucleation rates and lag times. We use maximum likelihood estimation (MLE) to analyze the nucleation and post-critical growth behavior. Given a list of times, $\{t_j\}$, at which a supercritical nucleus was first observed in a droplet, we seek to maximize the log-likelihood function

$$\log L = \sum_{j=1}^{n_{\text{obs}}} \log p(t_j) + (n_{\text{tot}} - n_{\text{obs}})\log p(t > t_{\text{max}}), \tag{27}$$

where $p(t)$ is the model probability of observing a supercritical nucleus at time t, n_{obs} is the number of observations ($j = 1, \ldots, n_{\text{obs}}$), and n_{tot} is the total number of droplets in the experiment.

A.1. Single nucleation rate. To begin, we assume that nucleation in all droplets can be described by a single rate, k_{n}. In this case, following the discussion in Sec. D.1, the probability of observing a supercritical nucleus in an experiment at time t is

$$p(t) = \int_0^t d(\Delta t)\,\text{IG}(\Delta t)k_{\text{n}}e^{-k_{\text{n}}(t-\Delta t)}. \tag{28}$$

The probability that a supercritical nucleus is not observed in a droplet before the end of the experiment at time t_{max} is

$$p(t > t_{\text{max}}) = \int_{t_{\text{max}}}^{\infty} dt \int_0^t d(\Delta t)\,\text{IG}(\Delta t; \mu_{\text{lag}}, D_{\text{lag}})k_{\text{n}}e^{-k_{\text{n}}(t-\Delta t)} \tag{29}$$

$$\simeq \int_{t_{\text{max}}}^{\infty} dt\, k_{\text{n}}e^{-k_{\text{n}}(t-t^*)} = e^{-k_{\text{n}}(t_{\text{max}}-t^*)}, \tag{30}$$

where we have defined

$$t^* \equiv \frac{1}{k_{\text{n}}}\log\int_0^{\infty} d(\Delta t)e^{k_{\text{n}}\Delta t}\text{IG}(\Delta t; \mu_{\text{lag}}, D_{\text{lag}}). \tag{31}$$

We fit this MLE model to the data from each concentration and temperature with k_{n}, μ_{lag}, and D_{lag} as fitting parameters. Figure S12 shows the raw parameters that we obtain, along with the predicted concentration scalings. The data collapse for k_{n} confirms that the nucleation rate prefactor is roughly linear in concentration and that the inferred nucleation barrier heights are well described by CNT. From the asymptotic behavior at high supersaturation, we find that $k_{\text{n},0}/V_{\text{drop}}\rho \simeq V_{\text{drop}}^{-1} \times \exp(22.4)\,\text{M}^{-1}\text{s}^{-1} \simeq 1 \times 10^{-4}\,\text{s}^{-1}$. Given that $\gamma\rho_{\text{c}}^{-2/3}$ is in the range of 1 to $2k_{\text{B}}T$, we use Eq. (12) to estimate that $k_{\text{att}}(S=1) \simeq 1 \times 10^{-4}\,\text{s}^{-1}$, which is close to our estimate from Eq. (8). Thus, the inferred nucleation-rate prefactor is consistent with our attachment-kinetics model to within an order of magnitude.

Analysis of the lag times shows that both μ_{lag} and D_{lag} collapse onto master curves when scaled by $\rho^{2/3}$, as expected from Eq. (22). Furthermore, the inferred diffusion coefficients are roughly constant as a function of supersaturation, which is consistent with the predictions of the kMC simulations shown in Figure S11. We also confirm that $D_{\text{lag}}/\mu_{\text{lag}}$ in the asymptotic regime of high supersaturation is of order 100, which is consistent with a minimum observable cluster size, N_{min}, of approximately 50–200 colloidal particles. Note that the uncertainty in the diffusion coefficients is large at low supersaturation because crystallization events were not observed in most of these droplets within the duration of the experiment.
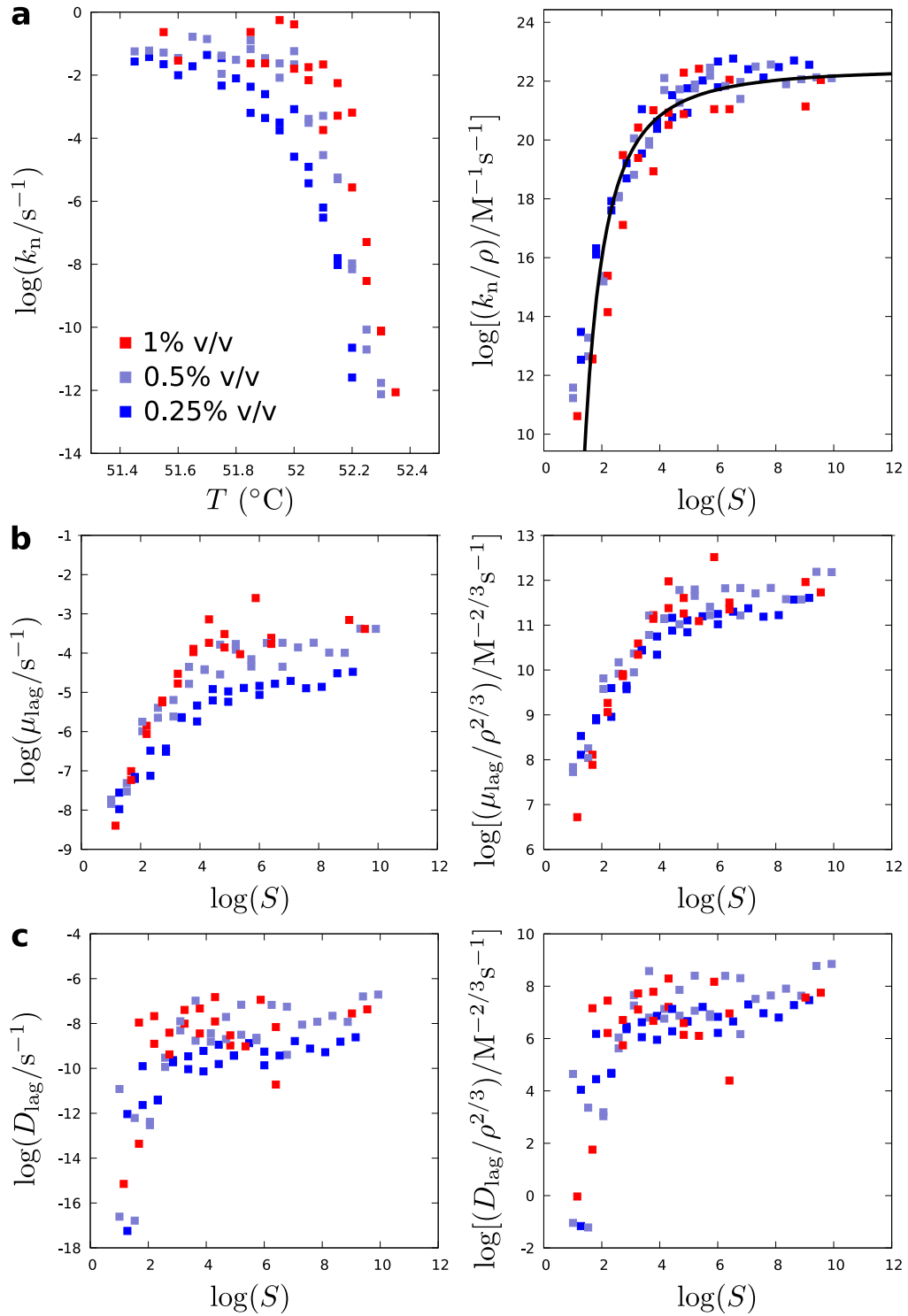
Fig. S12. Nucleation and early-time growth parameters determined from fits to the single-nucleation-rate MLE model described in Sec. A.1. The fitting parameters k_n, μ_{lag}, and D_{lag} are determined separately for each quench. Panels on the left show the raw data for the (**a**) nucleation rate, (**b**) lag time drift coefficient, and (**c**) lag time diffusion coefficient, while panels on the right show the rescaled data. In panel **a**(*right*), the black curve shows a fit to Eq. (32) with $k_{n,0} = \exp(22.4)$ and $B = 25.8$. The fit to the rescaled data in panel **b**(*right*) is shown in Figure S14a. The plateau in panel **c**(*right*) is consistent with the prediction of Figure S11 and is thus used to fix a supersaturation-independent D_{lag} in the variable-concentration fits described in Sec. A.2.

Alexander Hensley, William M. Jacobs, W. Benjamin Rogers

Nominal concentration (% v/v)	Mean concentration (M)	Standard deviation (M)	Δ
0.25	3.33×10^{-11}	0.30×10^{-11}	0.090
0.50	7.24×10^{-11}	0.49×10^{-11}	0.067
1.00	14.19×10^{-11}	0.58×10^{-11}	0.041

Table S3. Concentration measurements for the three nominal concentrations (cf. Figure S8).

A.2. Accounting for variable droplet concentrations. Now we account for variations in the colloid concentrations from droplet to droplet (see Table S3). We assume that the concentration in a randomly selected droplet follows a Gaussian distribution with mean $\bar{\rho}$ and standard deviation $\Delta\rho$. We define the mean supersaturation to be $\bar{S} \equiv \bar{\rho}/\rho_{\mathrm{eq}}(T)$ and the relative variation in concentrations to be $\Delta \equiv \Delta\rho/\bar{\rho}$. Assuming a CNT rate of the form

$$k_{\mathrm{n}}(\rho, S, B) = k_{\mathrm{n},0}\rho \exp\left[\frac{-B}{(\log S)^2}\right], \tag{32}$$

where B is a fitting parameter, the probability that a nucleation event occurs at time t in any of the droplets is

$$p_{\mathrm{nuc}}(t; \bar{S}, \Delta, B) = \int_{1/\bar{S}}^{\infty} d\zeta \left(\frac{e^{-(\zeta-1)^2/2\Delta^2}}{\sqrt{2\pi\Delta^2}}\right) k_{\mathrm{n}}(\zeta\rho_{\mathrm{eq}}\bar{S}, \zeta\bar{S}, B)e^{-k_{\mathrm{n}}(\zeta\rho_{\mathrm{eq}}\bar{S}, \zeta\bar{S}, B)t}, \tag{33}$$

where $\zeta \equiv \rho/\bar{\rho}$. The lower integration limit reflects the fact that nucleation can only occur when $\rho > \rho_{\mathrm{eq}}(T)$. The probability of observing a supercritical nucleus at time t is

$$p(t) = \int_0^t d(\Delta t)\mathrm{IG}(\Delta t)p_{\mathrm{nuc}}(t - \Delta t), \tag{34}$$

while the probability of not observing nucleation prior to the end of the experiment is

$$p(t > t_{\mathrm{max}}) = p_{\mathrm{never}} + \int_{t_{\mathrm{max}}}^{\infty} dt\, p(t), \tag{35}$$

where p_{never} is the probability that the concentration in a drop is at or below the coexistence concentration, $\rho \leq \rho_{\mathrm{eq}}(T)$,

$$p_{\mathrm{never}} = \int_{-\infty}^{1/\bar{S}} d\zeta \left(\frac{e^{-(\zeta-1)^2/2\Delta^2}}{\sqrt{2\pi\Delta^2}}\right). \tag{36}$$

In practice, we find that p_{never} is negligible for the values of $\bar{S}$ and Δ considered.
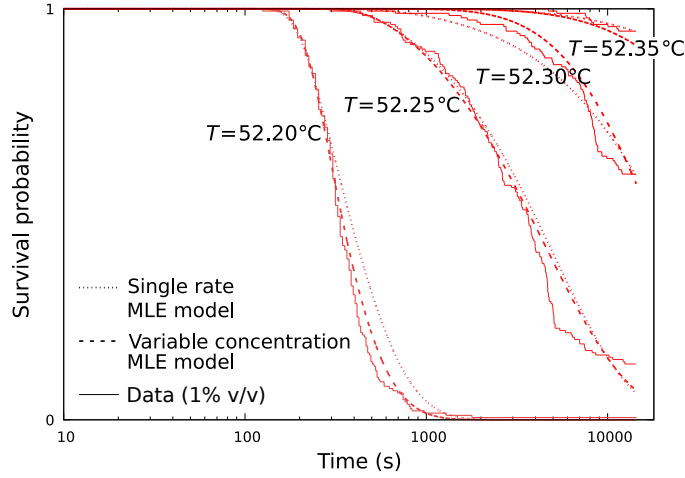
We fit this variable-concentration MLE model to the experimental data at all concentrations and temperatures. To reduce the number of fitting parameters, we impose a concentration-dependent D_{lag} and a single constant value of $k_{\mathrm{n},0}/\rho$, as determined from Figure S12c. The remaining fitting parameters are thus B and μ_{lag}. The results of this fitting procedure are shown in Figures 2 and 3 in the main text. We note that the difference between the two MLE models is most apparent at low average supersaturation. In this regime, the variation among CNT rates in droplets under the same nominal conditions is relatively large, and thus deviations from single-exponential nucleation rates become apparent. For visual comparison of these two models, representative predicted survival functions are shown along with the experimental survival functions in Figure S13.

We find that fixing a supersaturation-independent value of D_{lag}, as described above, tends to reduce the noise in the estimation of the mean lag times, $\tau_{\mathrm{lag}} = 1/\mu_{\mathrm{lag}}$. The lag time drift coefficients shown in Figure S14a correspond to the mean lag times shown in Figure 3c in the main text. The asymptotic value that we extract at high supersaturations, approximately $\mu_{\mathrm{lag}}/\rho^{2/3} \simeq 3 \times 10^5\,\mathrm{M}^{-2/3}\mathrm{s}^{-1}$, compares favorably with the prediction of Eq. (22), $\mu_{\mathrm{lag}}/\rho^{2/3} \sim \alpha D N_{\mathrm{min}}^{1/3} \simeq 5 \times 10^4\,\mathrm{M}^{-2/3}\mathrm{s}^{-1}$ in the limit $S \to \infty$. We are also able to extract the equilibrium constant $K \simeq 0.01S$ by fitting $\mu_{\mathrm{lag}}/\rho^{2/3}$ to Eq. (22). From this fit, we obtain inferred values of the attachment coefficient for post-critical nucleus growth, which are plotted in Figure S14b. The range of values obtained here, $0.01 \leq \langle\alpha\rangle_{\mathrm{post-critical}} \leq 1$, is consistent with the predicted cross-over from kinetics limited attachment at the critical nucleus to diffusion-limited growth at later times, when $R \gg d$ and thus $\alpha_{\mathrm{diff}} = (\pi/6\phi)d^2/\lambda R \ll 1$. We note that although the value of K/S obtained here is two orders of magnitude larger than the value of $k_{\mathrm{att}}(S = 1)$ obtained from the nucleation rate prefactor in Sec. A.1, this difference is expected, since the inference from the lag time data reflects an average over cluster sizes from the critical nucleus up to N_{min}. Thus, the larger average value of K/S obtained from the lag time data is consistent with Eq. (8), since the typical value of z' in the intermediate state of the attachment process increases as a post-critical nucleus grows and the curvature of the crystal–vapor interface decreases.

B. Interpretation of inferred surface tension values. According to the capillarity approximation, the quantity $[B(T)/(16\pi/3)]^{1/3}$ should be interpreted as the dimensionless surface tension, $\gamma(T)\rho_{\mathrm{c}}^{-2/3}/k_{\mathrm{B}}T$. Furthermore, at sufficiently low temperatures, $\gamma(T)\rho_{\mathrm{c}}^{-2/3}/k_{\mathrm{B}}T$ should be roughly equal to the free energy per unit surface area associated with half the missing "bonds" on a planar crystal–vapor interface. Thus, we expect

$$\frac{\gamma(T)\rho_{\mathrm{c}}^{-2/3}}{k_{\mathrm{B}}T} \simeq -\frac{z_{\mathrm{surf}}\varepsilon}{2k_{\mathrm{B}}T}, \tag{37}$$

where z_{surf} is the number of missing bonds within an interfacial region of area d^2. Figure 2f in the main text shows that this quantity is indeed roughly linear with respect to temperature, which is consistent with the temperature dependence predicted by Eq. (4) if $1 \lesssim z_{\mathrm{surf}} \lesssim 2$.

Fig. S13. Comparison of the single-nucleation-rate and variable-concentration MLE models at low supersaturation. In this regime, roughly $\log S \lesssim 2$, variations in the supersaturation across droplets at the same nominal concentration are not insignificant, and the differences between the best fits of the two MLE models are apparent. Both MLE models assume a constant value of $D_{\mathrm{lag}} = 0.0001\,\mathrm{s}^{-1}$ as described in the text.
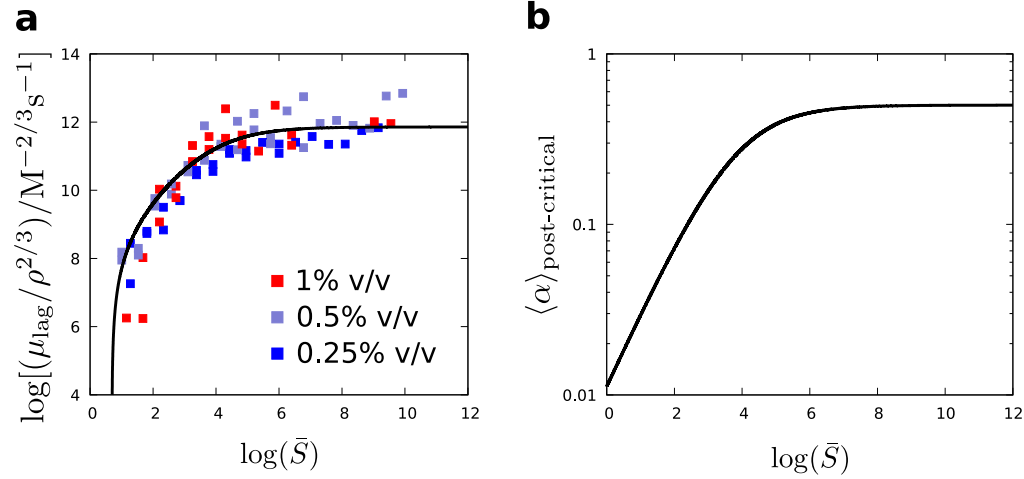
Fig. S14. The rescaled lag time drift coefficient obtained from fitting the variable-concentration MLE model described in Sec. A.2. (**a**) The data in this panel correspond to the lag times shown in Figure 3c in the main text. The black line is the fit to Eq. (22), which yields the estimate $K/S = 0.01$. (**b**) Given this estimate for K/S, we plot the inferred supersaturation-dependent attachment coefficient, which represents an average of the attachment coefficient over post-critical nuclei with fewer than N_{min} particles.

Furthermore, it appears that γ extrapolates to zero near 53°C; at this temperature, the cell model breaks down, since Eq. (2) predicts that the equilibrium gas density is comparable to ρ_c. This behavior is compatible with the expected phase diagram for hard-sphere square-well crystallization (4).

Nonetheless, the absolute values of $\gamma(T)\rho_c^{-2/3}/k_{\mathrm{B}}T$ inferred in this way are slightly lower than those predicted by Eq. (37). One likely culprit is the uncertainty associated with the interaction-range parameter δ used in predicting the absolute value of the binding free energy, as noted in Sec. A. Another contribution missing from this argument is the conformational entropy of a small critical nucleus, which may lead to substantial deviations from the low-temperature capillarity approximation. By applying the nucleation theorem, $i^* = \partial \Delta G^{\ddagger}/\partial \mu$, to the inferred barrier heights shown in Figure 2e in the main text, we estimate that the critical nucleus contains on the order of 10 colloids when $1 \lesssim \log(S) \lesssim 4$. Thus, substantial conformational fluctuations are likely to result in a roughly temperature-independent contribution to $\gamma/k_{\mathrm{B}}T$ obtained by fitting CNT, which assumes the capillarity approximation, to the data.

A third possibility is that the surface tension is being underestimated due to variations in the grafting density of DNA strands on the surface of the colloidal particles. These variations lead to a distribution of binding free energies, meaning that Eq. (4) only captures the mean binding free energy and not the interactions between all pairs of particles in a small cluster. In what follows, we show that binding-energy heterogeneity can lead to an apparent surface tension for small clusters that is lower than that of a macroscopic planar interface, and we estimate the magnitude of this effect. We assume that the bulk free energy per colloid in CNT follows a Gaussian distribution, $p(\Delta\mu)$, with mean $\overline{\Delta\mu}$ and variance s^2. Assuming that a randomly composed cluster of i colloids can be characterized by a classical free energy of the form $\Delta G/k_{\mathrm{B}}T = \theta i^{2/3} - \Delta\mu i$ and that there are no correlations between $\Delta\mu$ for the various colloids within a cluster, the resulting projected free

Alexander Hensley, William M. Jacobs, W. Benjamin Rogers

energy landscape as a function of cluster size is

$$\frac{\widetilde{\Delta G}(i)}{k_{\mathrm{B}}T} = -\log \int d\left(\frac{\Delta\mu i}{k_{\mathrm{B}}T}\right) p\left(\frac{\Delta\mu i}{kT}\right) \exp\left(-\theta i^{2/3} + \frac{\Delta\mu i}{kT}\right) = \theta i^{2/3} - \left[\left(\frac{\overline{\Delta\mu}}{k_{\mathrm{B}}T}\right) + \frac{1}{2}\left(\frac{s}{k_{\mathrm{B}}T}\right)^2\right] i. \tag{38}$$

The final term in this equation implies that variations in the bond energies decrease the critical barrier height, since $s^2 > 0$. The CNT barrier height is now

$$\frac{\widetilde{\Delta G}^{\ddagger}}{k_{\mathrm{B}}T} = \frac{-16\pi}{3} \frac{(\gamma\rho_{\mathrm{c}}^{-2/3}/k_{\mathrm{B}}T)^3}{\left[\log S + (s/k_{\mathrm{B}}T)^2/2\right]^2}. \tag{39}$$

Next, we estimate s^2 by assuming that the colloid–colloid binding free energies are independent. If we define the "patch-to-patch" polydispersity in the grafting density to be Δ_{g}, then we obtain $s^2 = z(\Delta_{\mathrm{g}}\bar{\varepsilon})^2$, where $\bar{\varepsilon}$ is the mean binding free energy. The effective surface tension appearing in Eq. (10) can therefore be written as

$$\gamma_{\mathrm{eff}} = \gamma\left[1 + \frac{z}{2\log S}\left(\frac{\Delta_{\mathrm{g}}\bar{\varepsilon}}{k_{\mathrm{B}}T}\right)^2\right]^{-2/3}. \tag{40}$$

Plugging in the estimated values $\Delta_{\mathrm{g}} \simeq 0.1$ and $\bar{\varepsilon} \simeq 4.5 k_{\mathrm{B}}T$, we find that γ_{eff} may be 20% smaller than γ when $\log S \simeq 2$. Note that this correction is largest at high temperatures, where the supersaturation is low in the experiments.

C. Fitting diffusion-limited growth. We infer an effective diffusion coefficient for each droplet concentration and temperature by fitting the trajectory of every droplet to the diffusion-limited growth model, Eq. (26), using an effective diffusion coefficient, $D_{\mathrm{eff}} \equiv D(1 - \alpha_{\mathrm{diff}}/\alpha)$, as a fitting parameter. Representative trajectories are shown in Figure 1F in the main text and shifted to account for the stochastic nucleation times in Figure S15. For a given concentration and temperature, we take the mean and standard deviation of the fitted diffusion coefficient of all droplets that formed a crystal and plot these results in Figure S16. For temperatures at which many crystals nucleate, we find that this effective diffusion coefficient is significantly higher than what is predicted by Stokes–Einstein, which we calculate to be $D_{SE} = 1.5 \times 10^{-12}$ m^2/s. This observation is likely a consequence of there being multiple crystals growing simultaneously within a single droplet, whereas Eq. (26) assumes a single spherical crystal. However, for quenches where only a single crystal nucleates in each droplet, we find that the fitted effective diffusion coefficient is within a factor of two of the predicted value, which is consistent with our model if $\alpha_{\mathrm{diff}}/\alpha \lesssim 0.5$ as expected for diffusion-limited growth. This match between our experiments and our model further supports the conclusion that the late stages of crystal growth are largely diffusion-limited.
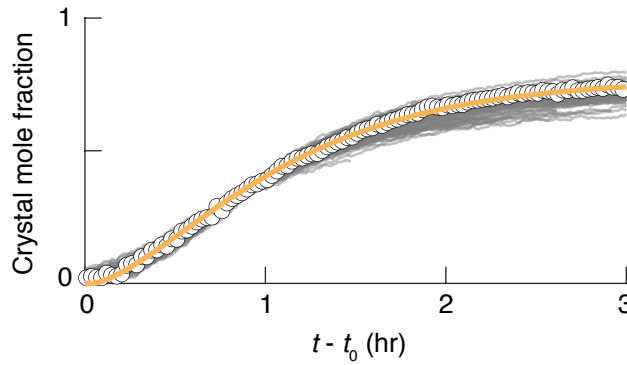

Fig. S15. Comparison of the growth curves for multiple droplets at the same temperature and colloid concentration. The graph shows the crystal mole fraction as a function of time since a crystal was detected t_0 for the same experiment shown in Figure 1F in the main text. All of the curves overlap one another, indicating that the crystal in each droplet follows the same growth behavior.

D. Predicting distributions of crystals per droplet via simulation. Based on our modeling of the nucleation and growth kinetics, we use a simple Monte-Carlo simulation to predict the distribution of the number of crystals grown within each droplet. To this end, we simulate 1000 droplets with the same initial nucleation rate k_{n} determined from the CNT-based analysis described above. We then evolve the system in discrete time steps of duration $\Delta t = 1$ s. For each time step, we determine whether or not a crystal nucleates within each drop during that time step by approximating the exponential waiting time distribution: A crystal nucleates within droplet i if $\Delta t k_{\mathrm{n}} < p_i$, where p_i is a uniform random number between 0 and 1. With $\Delta t = 1$ s, the probability of nucleation in a given time step for the deepest quenches is around 1% and is significantly lower for shallower quenches. After the initial nucleation event, the nucleation rate becomes time-dependent, since the growth of the crystal phase depletes the bulk concentration over time. We account for this effect by numerically integrating the rate of diffusion-limited growth, Eq. (26), of a spherical crystal over time in a droplet with a radius commensurate with those in the experiment. We calculate a new nucleation rate for each droplet at every time step after the first nucleation event and perform the same procedure to determine whether another crystal has nucleated. At the end of the simulation, we obtain the number of crystals that have nucleated within each droplet.
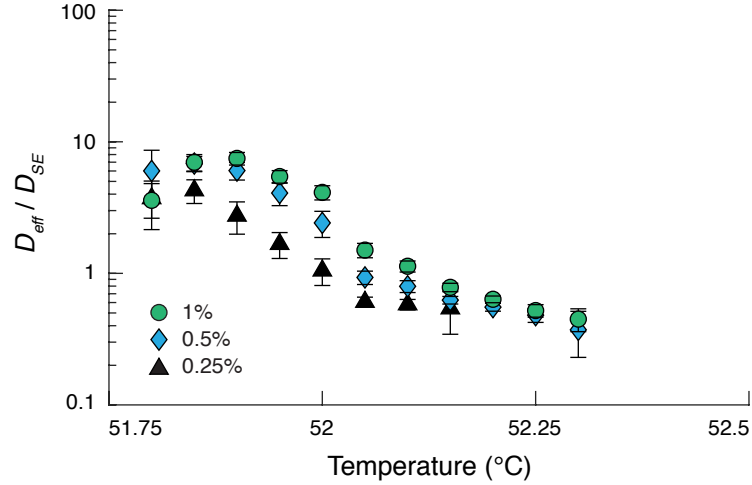
Fig. S16. The average effective diffusion coefficient of the crystal growth trajectories relative to the self-diffusion coefficient predicted by Stokes–Einstein, D_{SE}, as a function of temperature. For deep quenches, where many crystals nucleate, D_{eff} much larger than the self-diffusion coefficient due to the fact that multiple crystals are growing simultaneously. At higher temperatures, where mostly single crystals form, the effective diffusion coefficient is roughly half of the predicted self-diffusion coefficient.

These simulations confirm the intuition that the crystal morphology depends on a balance of nucleation and growth. In Figure S17, we show the distributions of the number of crystals that form per drop at three different supersaturations, and we note that the fraction of droplets that nucleate multiple crystals increases rapidly with increasing supersaturation. Overall, the simulations agree well with the experimental results, indicating that CNT is sufficient to explain the morphology of the crystals that self-assemble.
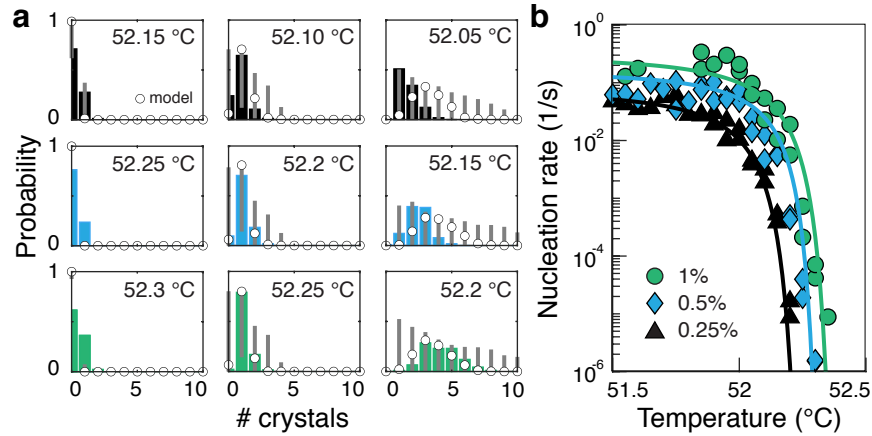
Fig. S17. The distributions of the number of crystal domains per droplet for three different colloid concentrations agree favorably with our model predictions of the coupled nucleation and growth of colloidal crystals. (**a**) shows the probability that a droplet contains a given number of crystals for three different colloids concentrations: 0.25% (black), 0.5% (blue), and 1% (green). For each concentration, we show the distributions for the three highest-temperature quenches where crystals nucleate. Colored bars show experimental data. White circles show model predictions, described in the text, for the nucleation rates given by the solid curves in **b**. The gray bars show the variability in the probability of forming a given number of crystals due to a variation in the surface tension γ of $\pm 10\%$. (**b**) shows the measured nucleation rates (points) and the corresponding model predictions (solid curves).

8. Predicting protocols for growing single crystals

A. Modeling isothermal crystallization. We now apply our model of the nucleation and growth dynamics for an individual nucleus to predict the conditions under which we can reliably grow single crystals. Based on the experiments and modeling discussed above, we know the nucleation rate as a function of the initial concentration and the temperature, $k_{\text{n}}(\rho_0, T)$. However, once an initial nucleus begins to grow, it will deplete the pool of available monomers and thus alter the nucleation rate elsewhere in the droplet. To simplify our analysis, we calculate a characteristic time, τ_{g}, which describes the time required for a single nucleus to grow large enough to suppress nucleation at the initial rate k_{n} elsewhere in the droplet. This definition implies that the probability that a new nucleus does *not* appear during the time interval τ_{g} is given by $\exp(-k_{\text{n}}\tau_{\text{g}})$. The probability of growing a single crystal in an isothermal experiment of duration $t_{\max} \gg \tau_{\text{g}}$ is thus given by

$$p_{1\text{x}} = \{1 - \exp[-k_{\text{n}}t_{\max}]\}\exp[-k_{\text{n}}\tau_{\text{g}}]. \tag{41}$$

Alexander Hensley, William M. Jacobs, W. Benjamin Rogers

This expression states that, to observe a single crystal, the first nucleus must appear within a time interval $t_{\max}$ and no other nucleus can appear within the following characteristic growth time τ_g.

In order to calculate τ_g, we equate the survival probability $\exp(-k_n \tau_g)$ to the probability of nucleating a second crystal in the full dynamical growth model, in which the instantaneous nucleation rate in the droplet changes with time. This condition implies

$$\exp\left[-k_n(\rho_0, T)\tau_g\right] = \exp\left\{-\int_0^\infty dt \, 4\pi V_{\text{drop}}^{-1} \int_{R(t)}^{R_{\text{drop}}} dr \, r^2 k_n[\rho(r,t), T]\right\}, \quad [42]$$

where t is the time since the appearance of the first nucleus, R is the radius of the first nucleus, R_{drop} is the droplet radius, and we've assumed that the first nucleus appears at the center of the droplet. We can therefore express τ_g as

$$\tau_g = \int_0^\infty dt \, \frac{\langle k_n \rangle_t}{k_n(\rho_0, T)}, \quad [43]$$

where $\langle k_n \rangle_t$ is the average nucleation rate in the droplet at time t. Because τ_g is much less sensitive to the initial concentration and temperature than the nucleation rate, we treat τ_g as a constant in the single-crystal probability calculations that follow.

We compare the predictions of this theory with the experimentally observed fraction of single crystals at a nominal 0.5% v/v concentration in Figure 4a in the main text. Assuming that crystal growth must have entered the diffusion-limited regime in order to suppress nucleation far away from the first nucleus, we use Eq. (13) to calculate $\rho(r,t)$. In this way, we estimate $\tau_g \simeq 500\,\text{s}$ near $T \simeq 52.3^\circ\text{C}$ using Eq. (43). These calculations also imply that $R(\tau_g) \simeq 3d$, which means that the crystal mole fraction should be approximately 0.02 when $t = \tau_g$; comparison with Figure 3d in the main text shows that this estimate of τ_g is consistent with our diffusion-limited growth data. Finally, we use this estimate of τ_g and the temperature-dependent nucleation rates to compute the single-crystal probability via Eq. (41). This prediction compares favorably with the experimental observations shown in Figure 4a in the main text. We caution that, due to limitations in detecting small crystals, the fraction of single crystals detected in our experiments may be a slight overestimate. Furthermore, we note that since there is some variation in the colloid concentrations across the droplets, the temperature window within which single crystals can form should be slightly broader than that predicted by our theory.

B. Modeling a time-dependent crystallization protocol. We now consider a crystallization protocol in which the quench is carried out according to a linear temperature ramp. Following our approach for calculating p_{1x} in isothermal experiments, we assume that τ_g is constant, while k_n is temperature-dependent. The probability of growing a single crystal using this linear-ramp protocol is

$$p_{1x}\left(\left|\frac{dT}{dt}\right|\right) = \left|\frac{dT}{dt}\right|^{-1} \int_0^\infty dT \, k_n(T) \exp\left[-\left|\frac{dT}{dt}\right|^{-1} \int_{T-(|dT/dt|)\tau_g}^\infty dT' \, k_n(T')\right], \quad [44]$$

where $|dT/dt|$ is the absolute value of the ramp rate. The predictions of this model compare favorably with experimental measurements using the nominal 0.5% v/v concentration, as shown in Figure 4b in the main text. We note that if an annealing protocol uses finite temperature steps instead of a continuous temperature ramp, then the probability of obtaining a single crystal may be lower than that predicted by Eq. (44). Furthermore, the probability of growing a single crystal using a protocol with finite temperature steps depends on the precise starting temperature in a non-monotonic fashion. Although our model of a continuous annealing protocol is not intended to account for these effects, we note that Eq. (44) remains a good approximation if the temperature steps are small compared to the temperature window over which single crystals can form.

As an additional check of our theory, we compare experimental results and model predictions for different droplet volumes. Intuitively, increasing the droplet volume increases the time that it takes for the nucleus to grow large enough to suppress nucleation elsewhere in the droplet. To determine how changing the droplet volume affects τ_g, we again assume that suppression of nucleation occurs within the diffusion-limited growth regime of the first nucleus. This assumption allows us to express $\langle k_n \rangle_t$ in terms of the ratio of $R(t)$ to R_{drop},

$$\langle k_n \rangle_t = 3 \int_{R(t)/R_{\text{drop}}}^1 dx \, x^2 k_n[\rho(x; R(t)/R_{\text{drop}}), T], \quad [45]$$

where $x \equiv r/R_{\text{drop}}$ and, according to Eq. (13), ρ depends only on x and $R(t)/R_{\text{drop}}$ if the initial nucleus is assumed to form at the center of the droplet. Using the fact that the crystal radius grows as $R \sim t^{1/2}$ in the diffusion-limited regime, Eq. (43) and Eq. (45) imply the scaling relation $\tau_g \sim V_{\text{drop}}^{2/3}$. With this scaling analysis, we can then use Eq. (44) to predict the single-crystal probability as a function of the droplet volume. The experimental results shown in figure S18 confirm that, at a fixed ramp rate, increasing the droplet volume indeed lowers the probability of forming a single crystal in a given droplet. Comparison of our theoretical predictions with these experimental results demonstrates that our theory accurately captures the functional dependence of τ_g, and thus the functional dependence of the single-crystal fraction, on the scaled droplet volume.

References

1. Oh JS, Wang Y, Pine DJ, Yi GR (2015) High-density PEO-b-DNA brushes on polymer particles for colloidal superstructures. *Chem. Mater.* 27(24):8337–8344.
2. Crocker JC, Grier DG (1996) Methods of digital video microscopy for colloidal studies. *Journal of Colloid and Interface Science* 179(1):298 – 310.
3. Wang Y, et al. (2015) Crystallization of DNA-coated colloids. *Nature Communications* 6:7253.
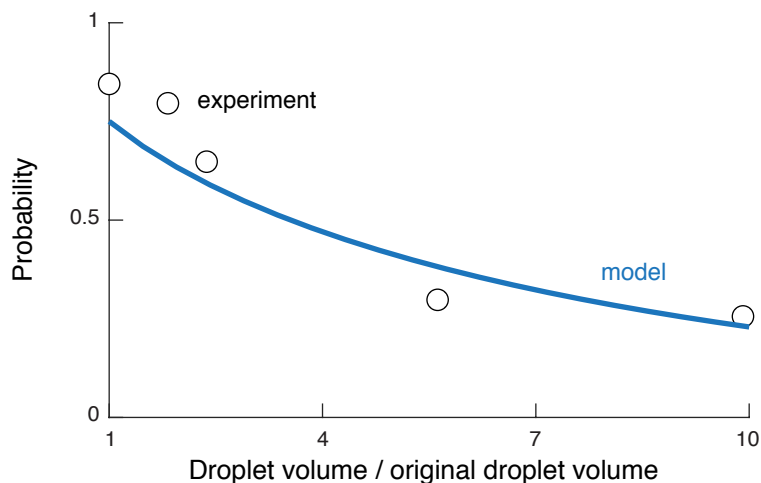
Fig. S18. Comparison of model predictions and experimental results of the probability of forming single crystals for droplets of different volumes. The graphs shows the probability of forming a single crystal within a droplet as a function of the relative droplet volume. The points show experimental measurements and the blue curve shows our model prediction. The original droplet radius is 27 micrometers, which is the same as the droplet radius in Figure 4b–c. Droplets with larger radii have a systematically lower probability of forming single crystals, as captured by our model predictions.

4. Charbonneau P, Frenkel D (2007) Gas-solid coexistence of adhesive spheres. *The Journal of Chemical Physics* 126(19):196101.
5. Rogers WB, Crocker JC (2011) Direct measurements of DNA-mediated colloidal interactions and their quantitative modeling. *Proceedings of the National Academy of Sciences of the United States of America* 108(38):15687–15692.
6. Lowensohn J, Oyarzún B, Paliza GN, Mognetti BM, Rogers WB (2019) Linker-mediated phase behavior of dna-coated colloids. *Physical Review X* 9(4):041054.
7. Palberg T (1999) Crystallization kinetics of repulsive colloidal spheres. *Journal of Physics: Condensed Matter* 11(28):R323.
8. Wang Y, et al. (2015) Crystallization of DNA-coated colloids. *Nature Communications* 6(1):7253.
9. Lee-Thorp JP, Holmes-Cerfon M (2018) Modeling the relative dynamics of DNA-coated colloids. *Soft Matter* 14(40):8147–8159.
10. Sear RP (2007) Nucleation: Theory and applications to protein solutions and colloidal suspensions. *Journal of Physics: Condensed Matter* 19(3):033101.
11. Oxtoby DW (1992) Homogeneous nucleation: theory and experiment. *Journal of Physics: Condensed Matter* 4(38):7627.
12. Libbrecht KG (2003) Growth rates of the principal facets of ice between $-10°C$ and $-40°C$. *Journal of Crystal Growth* 247(3-4):530–540.
13. Saito Y (1996) *Statistical physics of crystal growth.* (World Scientific).